Journal of Materials Chemistry A

PAPER

View Article Online
View Journal | View Issue

Cite this: J. Mater. Chem. A, 2014, 2, 14189

Triple-shelled Mn_2O_3 hollow nanocubes: force-induced synthesis and excellent performance as the anode in lithium-ion batteries†

H. B. Lin, H. B. Rong, W. Z. Huang, Y. H. Liao, L. D. Xing, M. Q. Xu, X. P. Li* and W. S. Li*

Received 28th May 2014
Accepted 11th July 2014

DOI: 10.1039/c4ta02666g

www.rsc.org/MaterialsA

In this paper, we report a novel structure of Mn_2O_3, the triple-shelled Mn_2O_3 hollow nanocube, as the anode material for high-energy lithium-ion batteries, synthesized through a programmed annealing treatment with cubic $MnCO_3$ as precursor. This hierarchical structure is developed through the interaction between the contraction force from the decomposition of $MnCO_3$ and the adhesion force from the formation of Mn_2O_3. The structure has been confirmed by characterization with XRD, FESEM, TEM, and HRTEM. The charge–discharge tests demonstrate that the resulting Mn_2O_3 exhibits excellent cycling stability and rate capability when evaluated as an anode material for lithium-ion batteries. It delivers a reversible capacity of 606 mA h g^{-1} at a current rate of 500 mA g^{-1} with a capacity retention of 88% and a remaining capacity of 350 mA h g^{-1} at 2000 mA g^{-1}.

Introduction

With the increasing demand for large-scale electrochemical energy storage, rechargeable lithium-ion batteries with a high-energy density, high rate capability and long-term stability are urgently required.[1,2] Transition metal oxides have been widely investigated as anodes in lithium-ion batteries because of their higher theoretical specific capacities compared with the commercial graphite anode currently available.[3–7] Among the various transition metal oxide anodes, Mn_2O_3 with a theoretical capacity of 1018 mA h g^{-1} is the most attractive owing to its abundance and environmentally friendly characteristics.[8–10] However, its major volume expansion during the charge–discharge process leads to a significant capacity loss and poor cycling stability, which greatly hinders its practical application in lithium-ion batteries.[11,12]

The synthesis of a hollow micro-/nanostructure with controlled size, shape and internal structure is a promising approach to improve the performance of transition metal oxide anodes.[13–16] The nano-size units reduce the path of lithium-ion diffusion and increase the number of reaction sites for lithium intercalation/deintercalation, and the interior hollow spaces buffer the volume changes during charge–discharge and thus enhance the rate capability and cyclic stability.[17–20] Much effort has been devoted to developing new strategies for rational synthesis of complex hollow structures, such as multi-shelled hollow structures and yolk–shelled structures, as these complex structures are expected to improve the properties of lithium-ion batteries.[21–24] A general approach for the fabrication of multi-shelled hollow structures involves the employment of sacrificial templates, such as monodispersed polymer,[25] silica,[13] or carbon.[26] However, methods employing sacrificial templates usually require multiple steps and post-treatment, which might not be suitable for cost-effective and environmentally-friendly large-scale manufacture. It is still a great challenge to develop a template-free method that enables facile synthesis of multi-shelled hollow structures.

In this paper, we report a novel structure of Mn_2O_3, the triple-shelled Mn_2O_3 hollow nanocube, synthesized through a programmed annealing treatment with cubic $MnCO_3$ as precursor. The crystal structure and morphology of the resulting product were characterized by XRD, FESEM, TEM, and HRTEM, and its performance as anode material in lithium-ion batteries, in terms of cyclic stability and capability, was evaluated with charge–discharge tests.

Experimental section

Material synthesis

The cubic $MnCO_3$ was synthesized by a precipitation reaction in a microemulsion.[27–29] Typically, 4 g of cetyltrimethyl ammonium bromide (CTAB) was dissolved in a mixture of 100 mL cyclohexane, 5 mL *n*-pentanol and 5 mL 0.8 M $(NH_4)HCO_3$ aqueous solution. The mixture was stirred for 20 min until it became transparent, then 5 mL 0.4 M $MnSO_4$ was dripped into the continuously stirred solution to produce a milky white

School of Chemistry and Environment, Key Laboratory of Electrochemical Technology on Energy Storage and Power Generation of Guangdong Higher Education Institutes, Engineering Research Center of Materials and Technology for Electrochemical Energy Storage (Ministry of Education), South China Normal University, Guangzhou, China. E-mail: liwsh@scnu.edu.cn; Fax: +86-20-39310256; Tel: +86-20-39310256

† Electronic supplementary information (ESI) available. See DOI: 10.1039/c4ta02666g

solution. Finally, the white $MnCO_3$ was filtered, washed several times with ethanol and distilled water, and dried in a vacuum at 90 °C. The triple-shelled Mn_2O_3 hollow nanocubes were synthesized by a two-step annealing process, using the cubic $MnCO_3$ as template. It was first sintered at 300 °C for 1 h with a ramping rate of 1 °C min^{-1} and then at 600 °C for 1 h with a ramping rate of 2 °C min^{-1} in air.

Materials characterization

The morphology of the materials was observed by field emission scanning electron microscopy (FESEM, ZEISS Ultra 55), transmission electron microscopy (TEM, JEOL JEM-2100HR) and high-resolution TEM (HRTEM). The crystal structures of the samples were analyzed by X-ray diffraction (XRD, BRUKER D8 ADVANCE, Germany) with Cu K_α radiation. The surface area was determined by the Brunauer–Emmett–Teller method (BET, Micromeritics ASAP 2020 M) at liquid nitrogen temperature (77 K).

Electrochemical measurements

The electrode was prepared by mixing 70 wt% active material with 20 wt% acetylene black and 10 wt% polyvinylidene difluoride (PVDF) binder, coating the mixture on an aluminum sheet, and then cutting the sheet into 1 cm × 1 cm samples. The typical mass of loaded active material was 5–7 mg. The CR2025 coin cell was assembled in an Ar-filled MBraun glove box using the prepared electrode as cathode, lithium film as anode, Celgard 2400 as separator, and 1 M $LiPF_6$ in ethylene carbonate (EC) and dimethyl carbonate (DMC) (EC/DMC 1 : 2 by volume) as electrolyte. The charge–discharge tests were performed on a Land cell test system (Land CT2001A, China). Cells were cycled between 3 V and 0.01 V (*vs.* Li/Li^+) at 25 °C. Cyclic voltammetry was performed on a Solartron-1470E CellTest at 25 °C between 3 V and 0.01 V at a sweep rate of 0.1 mV s^{-1}.

Results and discussion

Triple-shelled Mn_2O_3 hollow nanocubes are synthesized through a thermally driven contraction process during the decomposition of $MnCO_3$, a process which was developed in the fabrication of double-shelled $CoMn_2O_4$.[15] Uniform $MnCO_3$ nanocubes prepared by the microemulsion method are applied as the precursor.[27,28] The formation of Mn_2O_3 can be demonstrated by the thermogravimetric analysis curve for $MnCO_3$ nanocubes (Fig. S1†). Thermal decomposition in air leads to the conversion of $MnCO_3$ into manganese oxide, MnO_2, Mn_2O_3 or Mn_3O_4, depending upon the sintering temperature. The first steep weight loss (>300 °C) is associated with the decomposition of $MnCO_3$ to form MnO_2 phase, while the second steep weight loss (>490 °C) is the result of transformation of MnO_2 to Mn_2O_3. Usually, to obtain the pure phase of Mn_2O_3, as guided by the thermogravimetric analysis curve, thermal decomposition should be conducted at a temperature above 490 °C for a certain time. However, if the thermal decomposition process is simply stopped halfway, $MnCO_3$ can only be partially decomposed, which could lead to the development of a manganese oxide layer on the surface of the particles, whereas the inner cores should remain as $MnCO_3$.[30,31]

As illustrated in Fig. 1, the fabrication process mainly consists of two annealing treatment steps. The $MnCO_3$ nanocubes are first sintered at 300 °C for 1 h with a ramping rate of 1 °C min^{-1}, and partially converted into manganese oxide, leading to the formation of the first shell, which is mainly based on the heterogeneous contraction caused by non-equilibrium heat treatment.[15,16,32] During the calcination, a large temperature gradient (ΔT) is present along the radial direction, which leads to the formation of a manganese oxide shell on the surface of the $MnCO_3$ core.[32,33] There are two forces in opposite directions acting on the interface between the manganese oxide shell and the $MnCO_3$ core. One is the contraction force (F_c) as a result of the large weight loss during the calcinations, which promotes the inward shrinkage of the $MnCO_3$ core. The other is the adhesion force (F_a) from the relatively rigid shell, which prevents its inward contraction. With ΔT_1 at the first heat treatment, F_c exceeds F_a so that the inner core contracts inward and detaches from the outer shell. It can be observed that, after the first heat treatment, the particle maintains its cubic shape but its surface becomes coarser due to the release of CO_2 (Fig. S2A and B†). The TEM image of the product confirms the core–shell structure (Fig. S2C†). The XRD pattern provides evidence of the $MnCO_3$ core from the partially decomposed $MnCO_3$ nanocube (Fig. S2D†). Compared with the highly crystalline $MnCO_3$ (Fig. 2), the intensity of the XRD peaks decreased considerably upon partial decomposition of $MnCO_3$. This process was accompanied by a color change of the material from milky-white to brown (Fig. S3†). Similar to the first heat treatment, the product obtained was then annealed at 600 °C for 1 h with a ramping rate of 2 °C min^{-1}. The same process as the first heat treatment occurs in the precursor cube, leading to the formation of the second shell. When the heating is prolonged at high temperature, F_c decreases rapidly and F_a surpasses F_c, leading to the reversed direction for movement of materials. As a result, the inner core shrinks outward, leaving a hollow cavity in the center.

The as-synthesized samples were characterized by XRD to determine their crystallographic structure. As shown in Fig. 2, the resulting $MnCO_3$ exhibits a hexagonal phase (PDF#44-1472). All of the diffraction peaks of the Mn_2O_3 can be indexed to a cubic phase (PDF#73-1826) by comparing them with the standard pattern. No residues or contaminants have been detected in the two XRD patterns, indicating the high purity of the product.

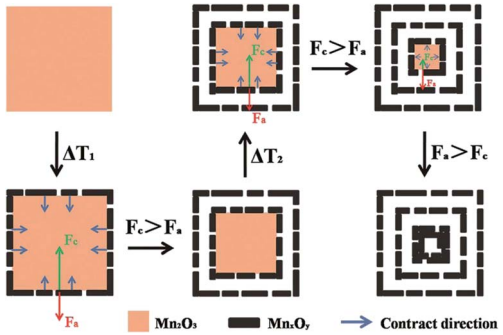

Fig. 1 Schematic illustration of the process of formation for triple-shelled Mn_2O_3 hollow nanocubes.

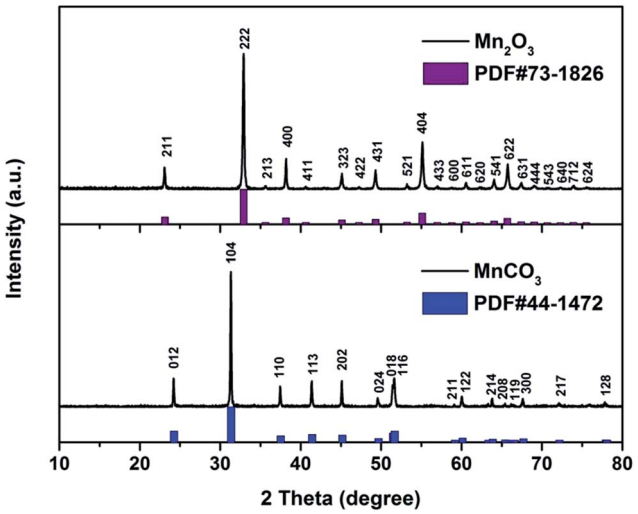

Fig. 2 XRD patterns for the $MnCO_3$ nanocube and the triple-shelled Mn_2O_3 hollow nanocube.

The morphology and detailed structure of the samples were observed by field-emission scan electron microscopy (FESEM) and transmission electron microscopy (TEM). As can be seen from Fig. 3A and B, the $MnCO_3$ obtained adopted a homogenous cubic shape with edge length of around 200 nm. When $MnSO_4$ and $(NH_4)_2CO_3$ solutions were mixed, $MnCO_3$ nucleated gradually in the microemulsion droplets. The selective interaction between the crystallographic planes of $MnCO_3$ and CTAB, which acts as a morphology controller,[27–29] resulted in the cubic shape and microemulsion defines the nanoparticle size. After the programmed heat treatment, the Mn_2O_3 product maintained the cubic shape, as shown in Fig. 3C. From the inset in Fig. 3C, it can be clearly observed that the Mn_2O_3 cube adopts a porous architecture composed of nanosized subunits. The porous structure is attributed to gas evolution from the $MnCO_3$ bulk during the thermal decomposition procedure to form manganese oxide. From the broken nanocubes with exfoliation of the shell as shown in Fig. 3D and E, the triple-shelled structure with the shell marked by the number and the hollow interior can be identified. Further FESEM images (Fig. S4†) indicate that the inner shells also retain the porous cubic shape. TEM images further confirmed the triple-shelled structure of the synthesized Mn_2O_3 nanocube. As shown in Fig. 3F and G, clear gaps can be distinguished between the shells, and the inner core can be confirmed to adopt the hollow cubic structure. Fig. 3H presents the high-resolution TEM (HRTEM) image of the Mn_2O_3 nanocube. The lattice fringes with interplanar spacing of about 0.54 nm can be indexed to the family of the (111) plane. The inset is the corresponding fast Fourier-transformed (FFT) pattern, indicating that the Mn_2O_3 nanocube adopts a highly crystalline structure. The BET result illustrated in Fig. 4 indicates that the pore sizes of triple-shelled Mn_2O_3 hollow nanocubes are mainly less than 30 nm, contributing to a surface area of 21.18 $m^2\ g^{-1}$.

The electrochemical properties of the triple-shelled Mn_2O_3 hollow nanocube were investigated in coin cells by both cyclic voltammetry and galvanostatic charge–discharge test using a lithium plate as reference and counter electrodes. The product obtained was first evaluated by cyclic voltammetry in the voltage range 0.01–3.0 V at a scan rate of 0.1 mV s^{-1}, as shown in Fig. 5A. During the first cathodic process, three main peaks were present centered at 1.25 V, 0.75 V and 0.2 V. The peaks located at 1.25 V and 0.2 V are attributed to the reduction of Mn^{3+} to Mn^{2+} and Mn^{2+} to Mn^0, respectively,[9,10] whereas the peak at 0.75 V is ascribed to the irreversible decomposition of the solvent in the electrolyte to form the solid–electrolyte interface (SEI).[16] The minor peak located at around 0.9 V may be attributed to the lithium-ion insertion into the conductive agent acetylene

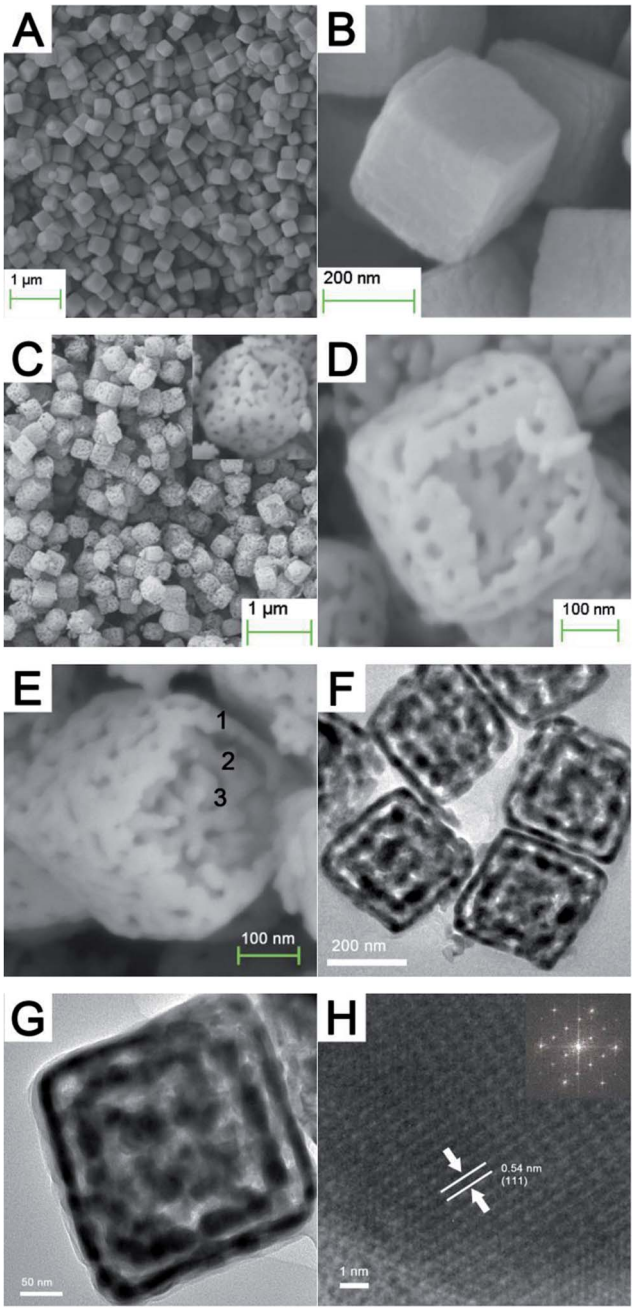

Fig. 3 FESEM images for the $MnCO_3$ nanocube (A and B), and FESEM (C–E), TEM (F and G) and HRTEM (H) images for the triple-shelled Mn_2O_3 hollow nanocube.

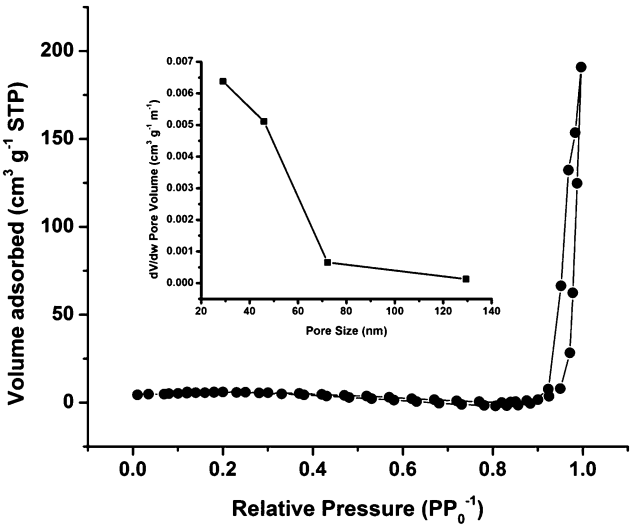

Fig. 4 N_2 adsorption/desorption isotherm for the triple-shelled Mn_2O_3 hollow nanocube and the corresponding pore size distribution.

black.[8,34] There are two oxidation peaks at 1.25 V and 2.35 V in the following anodic process, which are associated with the oxidation of Mn^0 to Mn^{2+} and Mn^{2+} to Mn^{3+}, respectively. Compared with the first cycle, two major peaks are observed in the following cycles, which correspond to the reduction/oxidation of Mn^{2+}. Note that the third curve and the fifth one overlap, indicating the good reversibility of the electrochemical reaction.

Fig. 5B and C illustrate the cycling performance of the triple-shelled Mn_2O_3 hollow nanocube at 100 mA g^{-1} current density between 3.0 V and 0.01 V and the corresponding discharge–charge profiles. The initial discharge and charge capacities are 1200 mA h g^{-1} and 845 mA h g^{-1}, respectively. The irreversible capacity loss of the first cycle can be attributed to the formation of the SEI film and the irreversible change between Mn^{3+} and Mn^{2+}, which correspond to the capacity in the voltage range between 1.5 V and 0.5 V. In the first discharge curve, two plateaus at around 1.3 V and 0.25 V could be attributed to the reduction of Mn^{3+} to Mn^{2+} and Mn^{2+} to Mn^0 and the plateaus at about 1.3 V and 2.4 V could be associated with the oxidation of Mn^0 to Mn^{2+} and Mn^{2+} to Mn^{3+}, respectively. After the first cycle, there are two main plateaus located at around 0.5 V and 1.5 V for the discharge and charge profiles, respectively, which are related to the Mn^{2+}/Mn^0 redox reaction. This result is consistent with observations from cyclic voltammetry.

It is well known that the major volume expansion of transition metal oxide anodes during the charge–discharge process leads to serious capacity loss and poor cycling stability. The cyclic stability of the resulting triple-shelled Mn_2O_3 hollow nanocube was evaluated with 100 charge–discharge cycles at current densities of 200 mA g^{-1} and 500 mA g^{-1} in the voltage range of 0.01–3.0 V. Fig. 6 presents the discharge capacity as a function of cycle number. All of the cells were first charged and discharged at a current density of 100 mA g^{-1} for two cycles. The first discharge capacity is around 718 mA h g^{-1} for the current density of 200 mA g^{-1} and 606 mA h g^{-1} for 500 mA g^{-1}. Interestingly, the discharge capacities gradually decrease and

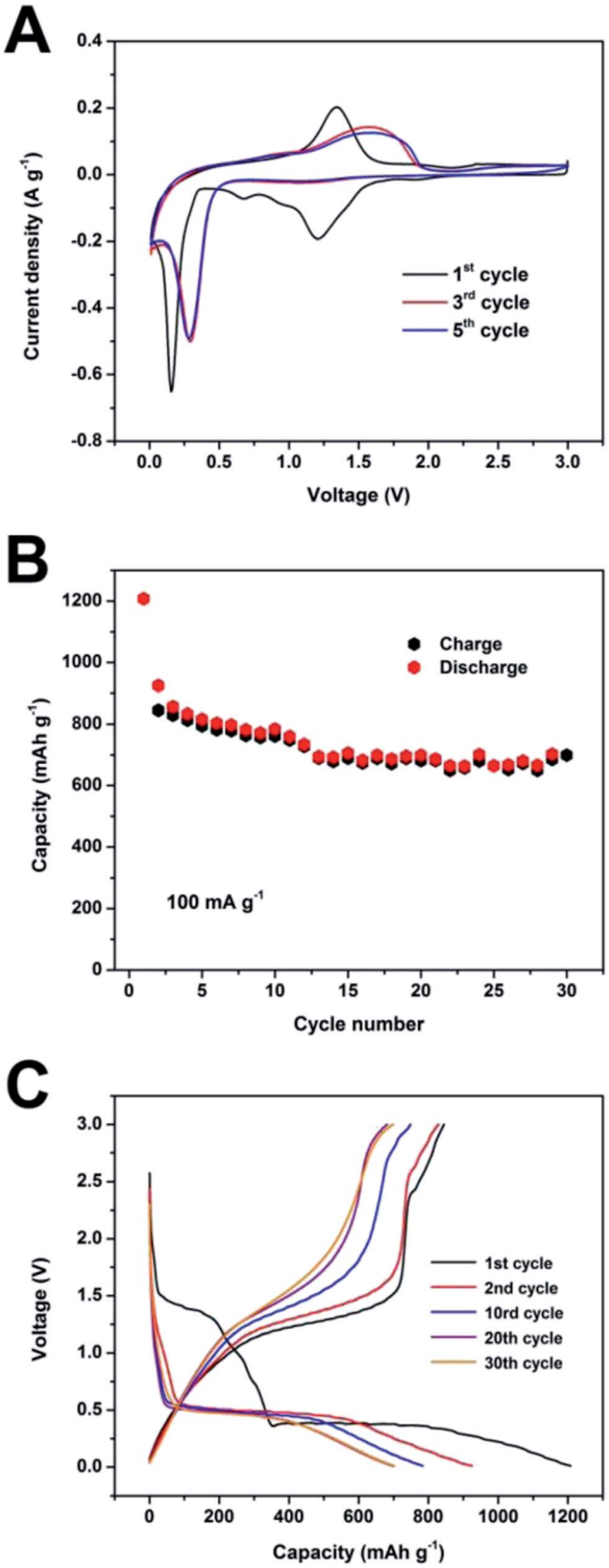

Fig. 5 (A) Cyclic voltammograms for the triple-shelled Mn_2O_3 nanocube electrode at a scan rate of 0.1 mV s^{-1} in the voltage range of 0.01–3.0 V. (B) Cycling performance in the voltage range of 0.01–3.0 V at a current density of 100 mA g^{-1} and (C) the corresponding discharge–charge profiles.

then start to increase after certain cycles. This phenomenon can be attributed to the presence of a possible activation process in the electrode, which is commonly observed for transition metal oxides.[4] Note that the discharge capacities stay above the specific capacity of graphite (372 mA h g^{-1}), although they change slightly. The discharge capacity at 500 mA g^{-1} remains 533 mA h g^{-1} after 100 cycles with a capacity retention of 88%, indicative of the excellent cyclic stability of the triple-shelled Mn_2O_3 hollow nanocube. This excellent cyclic stability should be related to the structural stability of the triple-shelled Mn_2O_3 hollow nanocube. Fig. 7 presents the FESEM images of the electrode after cycling. Compared with the image for the pristine nanoparticles (Fig. 3D), the porous cubic structure is maintained after cycling although the cube size increases slightly due to the SEI layer formed, confirming the structural stability of the triple-shelled Mn_2O_3 hollow nanocube. Apparently, the hierarchical structure of Mn_2O_3 provides space to buffer the mechanical strain induced by the volume change resulting from lithium insertion/extraction, maintaining the structural stability of Mn_2O_3.

To evaluate the rate capability, the resulting triple-shelled Mn_2O_3 hollow nanocube was cycled at various current densities ranging from 100 mA g^{-1} to 2000 mA g^{-1}. Fig. 8A and B show the rate capability of the triple-shelled Mn_2O_3 hollow nanocube and the corresponding discharge–charge profiles. The triple-shelled Mn_2O_3 hollow nanocube delivers a capacity of 350 mA h g^{-1} at 2000 mA g^{-1}. To the best of our knowledge, this is one of the best rate performances for Mn_2O_3 anodes that have been reported in the literature.[8,9,35] This excellent rate capability should be related to the nano-size units of Mn_2O_3. It should be noted that the discharge capacity recovers to 700 mA h g^{-1} when the current rate is returned back to 200 mA g^{-1}. These results indicate that the resulting triple-shelled Mn_2O_3 hollow nanocube simultaneously exhibits excellent cyclic stability and rate capability.

The excellent performance of the resulting triple-shelled Mn_2O_3 hollow nanocube can be attributed to its special structure. The hollow space buffers the mechanical strain induced by the volume change during cycling, while the nano-size units reduce the path of lithium-ion diffusion and increase the number of reaction sites for lithium insertion/extraction,

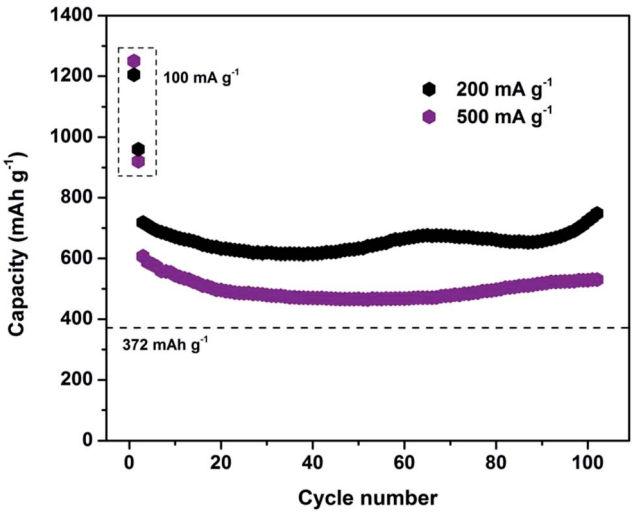

Fig. 6 Cyclic stability of the triple-shelled Mn_2O_3 nanocube electrode at current densities of 200 and 500 mA g^{-1}.

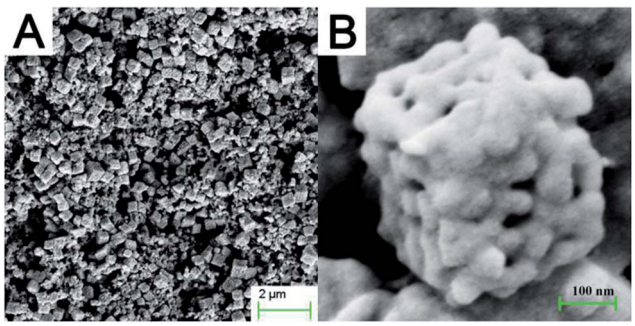

Fig. 7 FESEM images of the triple-shelled Mn_2O_3 nanocube electrode after cycling. (B) is a higher magnification FESEM image.

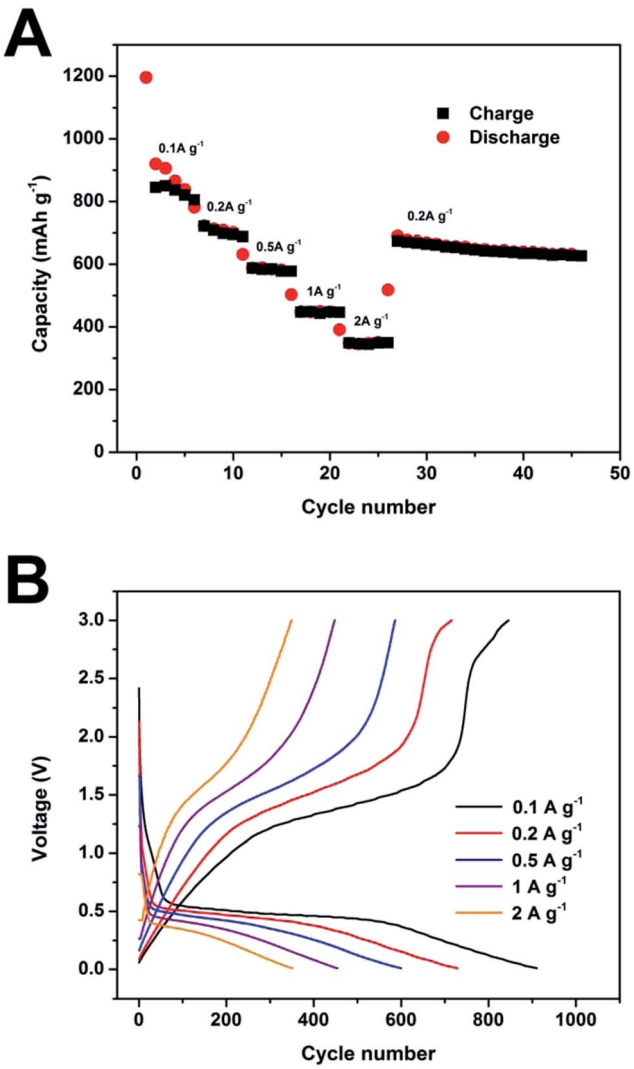

Fig. 8 (A) Specific capacity as a function of cycle number at different current densities and (B) the corresponding discharge–charge profiles.

leading to the excellent cyclic stability and rate capability of the resulting triple-shelled Mn_2O_3 hollow nanocube.

Conclusions

In summary, we have developed a novel structure of Mn_2O_3, the triple-shelled Mn_2O_3 hollow nanocube with nanosize subunits, as the anode material for high-energy lithium-ion batteries. The nanocube was synthesized through a programmed annealing treatment with cubic $MnCO_3$ as precursor. The resulting hierarchical structure is formed *via* the interaction between the contraction force from the decomposition of $MnCO_3$ and the adhesion force from the formation of Mn_2O_3. When evaluated as an anode material for lithium-ion batteries, the triple-shelled Mn_2O_3 hollow nanocube exhibits excellent cyclic stability and rate capability. The hollow space buffers the mechanical strain induced by the volume change during cycling, while the nanosize units reduce the path of lithium-ion diffusion and increase the number of reaction sites for lithium insertion/extraction, leading to the excellent cyclic stability and rate capability of the resulting triple-shelled Mn_2O_3 hollow nanocube.

Acknowledgements

This work is financially supported from the joint project of the National Natural Science Foundation of China and the Natural Science Foundation of Guangdong Province (Grant no. U1134002), the National Natural Science Foundation (Grant no. 21273084), the Natural Science Fund of Guangdong Province (Grant no. 10351063101000001), the key project of Science and Technology in Guangdong Province (Grant no. 2012A010702003), and the scientific research project of the Department of Education of Guangdong Province (Grant no. 2013CXZDA013).

Notes and references

1 N. S. Choi, Z. Chen, S. A. Freunberger, X. Ji, Y. K. Sun, K. Amine, G. Yushin, L. F. Nazar, J. Cho and P. G. Bruce, *Angew. Chem., Int. Ed.*, 2012, **51**, 9994–10024.
2 X. W. Lou, L. A. Archer and Z. Yang, *Adv. Mater.*, 2008, **20**, 3987–4019.
3 X. W. Lou, D. Deng, J. Y. Lee, J. Feng and L. A. Archer, *Adv. Mater.*, 2008, **20**, 258–262.
4 C. Wu, X. Li, W. Li, B. Li, Y. Wang, Y. Wang, M. Xu and L. Xing, *J. Power Sources*, 2014, **251**, 85–91.
5 J. Lei, W. Li, X. Li and L. Zeng, *J. Power Sources*, 2013, **242**, 838–843.
6 J. F. Lei, L. B. Li, X. H. Shen, K. Du, J. Ni, C. J. Liu and W. S. Li, *Langmuir*, 2013, **29**, 13975–13981.
7 L. Zhou, H. Xu, H. Zhang, J. Yang, S. B. Hartono, K. Qian, J. Zou and C. Yu, *Chem. Commun.*, 2013, **49**, 8695–8697.
8 Y. Deng, Z. Li, Z. Shi, H. Xu, F. Peng and G. Chen, *RSC Adv.*, 2012, **2**, 4645–4647.
9 Y. Qiu, G.-L. Xu, K. Yan, H. Sun, J. Xiao, S. Yang, S.-G. Sun, L. Jin and H. Deng, *J. Mater. Chem.*, 2011, **21**, 6346.
10 X. Fang, X. Lu, X. Guo, Y. Mao, Y.-S. Hu, J. Wang, Z. Wang, F. Wu, H. Liu and L. Chen, *Electrochem. Commun.*, 2010, **12**, 1520–1523.
11 J. Guo, Q. Liu, C. Wang and M. R. Zachariah, *Adv. Funct. Mater.*, 2012, **22**, 803–811.
12 Y. Sun, X. Hu, W. Luo, F. Xia and Y. Huang, *Adv. Funct. Mater.*, 2013, **23**, 2436–2444.
13 X. W. Lou, C. M. Li and L. A. Archer, *Adv. Mater.*, 2009, **21**, 2536–2539.
14 Z. Wang and X. W. Lou, *Adv. Mater.*, 2012, **24**, 4124–4129.
15 G. Zhang, L. Yu, H. B. Wu, H. E. Hoster and X. W. Lou, *Adv. Mater.*, 2012, **24**, 4609–4613.
16 L. Zhou, D. Zhao and X. W. Lou, *Adv. Mater.*, 2012, **24**, 745–748.
17 Z. Wang, L. Zhou and X. W. Lou, *Adv. Mater.*, 2012, **24**, 1903–1911.
18 B. Wang, H. B. Wu, L. Zhang and X. W. Lou, *Angew. Chem., Int. Ed.*, 2013, **52**, 4165–4168.
19 L. Zhou, D. Zhao and X. W. Lou, *Angew. Chem., Int. Ed.*, 2012, **51**, 239–241.
20 H. B. Lin, Y. M. Zhang, J. N. Hu, Y. T. Wang, L. D. Xing, M. Q. Xu, X. P. Li and W. S. Li, *J. Power Sources*, 2014, **257**, 37–44.
21 X. Wang, X.-L. Wu, Y.-G. Guo, Y. Zhong, X. Cao, Y. Ma and J. Yao, *Adv. Funct. Mater.*, 2010, **20**, 1680–1686.
22 X.-J. Wu and D. Xu, *Adv. Mater.*, 2010, **22**, 1516–1520.
23 S. Yang, X. Feng, L. Zhi, Q. Cao, J. Maier and K. Muellen, *Adv. Mater.*, 2010, **22**, 838–842.
24 L. Yu, H. B. Wu and X. W. Lou, *Adv. Mater.*, 2013, **25**, 2296–2300.
25 M. Yang, J. Ma, C. Zhang, Z. Yang and Y. Lu, *Angew. Chem., Int. Ed.*, 2005, **44**, 6727–6730.
26 X. Lai, J. Li, B. A. Korgel, Z. Dong, Z. Li, F. Su, J. Du and D. Wang, *Angew. Chem., Int. Ed.*, 2011, **50**, 2738–2741.
27 X. Duan, J. Lian, J. Ma, T. Kim and W. Zheng, *Cryst. Growth Des.*, 2010, **10**, 4449–4455.
28 X. Wu, M. Cao, H. Lü, X. He and C. Hu, *J. Nanosci. Nanotechnol.*, 2006, **6**, 2123–2128.
29 H. B. Lin, J. N. Hu, H. B. Rong, Y. M. Zhang, S. W. Mai, L. D. Xing, M. Q. Xu, X. P. Li and W. S. Li, *J. Mater. Chem. A*, 2014, **2**, 9272–9279.
30 L. Wang, F. Tang, K. Ozawa, Z. G. Chen, A. Mukherj, Y. Zhu, J. Zou, H. M. Cheng and G. Q. Lu, *Angew. Chem., Int. Ed.*, 2009, **48**, 7048–7051.
31 L. Zhou, X. Zhou, X. Huang, Z. Liu, D. Zhao, X. Yao and C. Yu, *J. Mater. Chem. A*, 2013, **1**, 837–842.
32 J. Guan, F. Mou, Z. Sun and W. Shi, *Chem. Commun.*, 2010, **46**, 6605–6607.
33 F.-z. Mou, J.-g. Guan, Z.-g. Sun, X.-a. Fan and G.-x. Tong, *J. Solid State Chem.*, 2010, **183**, 736–743.
34 J. Shu, M. Shui, F. Huang, D. Xu, Y. Ren, L. Hou, J. Cui and J. Xu, *J. Phys. Chem. C*, 2011, **115**, 6954–6960.
35 L. Hu, Y. Sun, F. Zhang and Q. Chen, *J. Alloys Compd.*, 2013, **576**, 86–92.

